

Article

Determining Interface Fracture Toughness in Multi Layered Environmental Barrier Coatings with Laser Textured Silicon Bond Coat

Markus Wolf ^{1,*}, Hideki Kakisawa ², Fabia Süß ³, Daniel Emil Mack ¹  and Robert Vaßen ¹ 

¹ Forschungszentrum Jülich GmbH, Institute of Energy and Climate Research, Materials Synthesis and Processing (IEK-1), 52425 Jülich, Germany; d.e.mack@fz-juelich.de (D.E.M.); r.vassen@fz-juelich.de (R.V.)

² National Institute for Material Science, Research Center for Structural Materials (RCSM), Tsukuba Ibariki 305-0047, Japan; KAKISAWA.Hideki@nims.go.jp

³ German Aerospace Center (DLR), Institute of Structures and Design (BT), 70569 Stuttgart, Germany; Fabia.Suess@dlr.de

* Correspondence: m.wolf@fz-juelich.de

Abstract: In the high temperature combustion atmosphere inside of aircraft turbines, the currently used ceramic matrix composites require a protective environmental barrier coating (EBC) to mitigate corrosion of the turbine parts. Besides thermomechanical and thermochemical properties like matching thermal expansion coefficient (CTE) and a high resistance against corrosive media, mechanical properties like a high adhesion strength are also necessary for a long lifetime of the EBC. In the present work, the adhesion between an air plasma sprayed silicon bond coat and a vacuum plasma sprayed ytterbium disilicate topcoat was aimed to be enhanced by a laser surface structuring of the Si bond coat. An increase in interface toughness was assumed, since the introduction of structures would lead to an increased mechanical interlocking at the rougher bond coat interface. The interface toughness was measured by a new testing method, which allows the testing of specific interfaces. The results demonstrate a clear increase of the toughness from an original bond coat/topcoat interface (8.6 J/m²) compared to a laser structured interface (14.7 J/m²). Observations in the crack propagation indicates that the laser structuring may have led to a strengthening of the upper bond coat area by sintering. Furthermore, in addition to cohesive failure components, adhesive components can also be observed, which could have influenced the determined toughness.

Keywords: environmental barrier coatings (EBC); laser structuring; interface toughness; mechanical properties



Citation: Wolf, M.; Kakisawa, H.; Süß, F.; Mack, D.E.; Vaßen, R. Determining Interface Fracture Toughness in Multi Layered Environmental Barrier Coatings with Laser Textured Silicon Bond Coat. *Coatings* **2021**, *11*, 55. <https://doi.org/10.3390/coatings11010055>

Received: 27 November 2020

Accepted: 28 December 2020

Published: 6 January 2021

Publisher's Note: MDPI stays neutral with regard to jurisdictional claims in published maps and institutional affiliations.



Copyright: © 2021 by the authors. Licensee MDPI, Basel, Switzerland. This article is an open access article distributed under the terms and conditions of the Creative Commons Attribution (CC BY) license (<https://creativecommons.org/licenses/by/4.0/>).

1. Introduction

Gas turbines are commonly used in the field of power generation and aero engines. The currently used nickel-based alloys inside of the turbines, are limited in their operation temperature and require complex cooling and protection systems to operate at high temperatures. For this reason, new materials like SiC/SiC ceramic matrix composites (CMCs) are now in focus of the turbine development to achieve higher fuel efficiencies and to simultaneously reduce the release of environmentally harmful by-products [1–4]. These materials offer some advantages against the nickel-based alloys, such as much higher operation temperatures, lower weight, and superior mechanical properties [5–7]. However, despite these advantages, the SiC/SiC CMCs are vulnerable to corrosion by water vapor and calcium-magnesium-aluminosilicate (CMAS) at high temperature [8]. Therefore, it is necessary to protect the CMCs with environmental barrier coatings (EBCs).

The state-of-the-art materials for a 3rd generation EBC are the rare earth silicates of Ytterbium, Yttrium, or Lutetium. As Lutetium is too expensive for use in an industrial application and Yttrium silicates show temperature-dependent phase transformations,

Ytterbium silicate, especially Ytterbium disilicate (YbDS), as the topcoat material is more suitable. An advantage of the disilicates compared to their monosilicate counterparts is the smaller mismatch in the thermal expansion with the SiC/SiC CMC resulting in reduced stresses during thermal cycling [9–13]. The EBCs can be applied by various chemical (chemical vapor deposition), physical (physical vapor deposition), or thermal (plasma spray) deposition methods. In addition to the topcoats, typically a thermally sprayed silicon layer is used as a bond coat. The advantages of the plasma spray methods, which were used in this present work, are an inexpensive deposition of dense and thick coatings [14,15]. Bakan et al. [16] demonstrated in their work that it is possible to manufacture dense, crack-free coatings with a high crystallinity using the vacuum plasma spray technique.

Besides thermomechanical and thermochemical properties of EBC materials like a well matching CTE, a high resistance against corrosive medias, and a high temperature stability, another focus of development is on mechanical properties like a high interface fracture toughness and a high adhesion strength between top and bond coat layer or between the substrate and bond coat. These properties also have high impact on resistance against mechanical spallation and on the lifetime of the coatings [17].

Surface preparations such as grid blasting, grinding, roughening by waterjet or the application of additional bond coats are conventionally used to increase the roughness of the substrate for an improved adhesion of thermally sprayed coatings [18–21]. Drawbacks of these treatments are the possibilities to contaminate the substrate, e.g., by the grid blasting material and the erosive effect on the brittle ceramics. For these reasons, laser surface structuring attracts interest as a surface treatment for ceramics and CMCs [22–24]. Laser structuring offers the possibility to modify a surface quickly, with negligible residual deformations and only temporally low thermal alteration. In addition, the laser surface treatment is integrable to the coating procedure without any sample remounting, which also reduces the process time [21,25]. Challenges of laser structuring lie in precise process control to design the inserted structures at an optimal angle and depth. Improperly designed structures may not be completely filled by the applied topcoat material, which could create a weak point at the interface. Furthermore, the oxidation of the material to be patterned must be kept under control during the laser treatment, since an oxide layer could constitute another weak point in the coating system. Compared to other surface treatments, the acquisition of the equipment is significantly more expensive, but less expensive to maintain and use.

Various test methods have been suggested to characterise the interface toughness or the adhesion strength of coatings [26,27]. Conventional methods to test the adhesion strength or the interface toughness are, e.g., the pull off test, the single leg bending test [28,29], or the three-point bending test [30]. The collection of valid data from pull off adhesion tests depends on the strength and stability of the typical organic adhesives, which limits the tests to 70 MPa. In addition, all these tests measure the minimum adhesion strength or interface toughness within a whole coating system, including the substrate. With conventional methods, it is not possible to test a specific interface in a multilayer coating system.

To overcome these limits, new methods were developed. One new testing method, the laser shock adhesion test (LASAT), is presented by Berthe et al. [31]. This testing method is a powerful new approach of measuring the coating adhesion due to its easiness, speed, and ability to distinguish between various strength levels [18]. Another promising approach is presented by Kakisawa et al. [32], which allows the testing of a specific interface with a simple specimen geometry and without any adhesives. Especially the ability to test a specific interface and not the whole coating system is favourable. To test the interface toughness, a metallic wedge introduces stress concentration in a mode I rich condition at the interface until a crack growth is observable. Further, Kakisawa recently proposed a modified simple test method with a stiffener adhered on the coating [33].

In the present work the method developed by Kakisawa et al. [33] was used to examine the impact of a laser structured bond coat on the interface toughness of the Si bond coat/YbDS topcoat interface. A laser surface treatment was performed to alter mechanical

interlocking and local stress distributions to achieve an increased interface toughness. The impact of two geometric variations on the interface toughness was examined. The suitability of the testing method for the investigation of the interface toughness of structured interfaces is discussed.

2. Materials and Methods

2.1. Materials

100 mm × 40 mm × 2 mm SiC/SiCN substrates were manufactured via polymer infiltration and pyrolysis process at the DLR Stuttgart: Tyranno SA3 plain weave fabric layers were stacked on top of each other into a mould. The fibre volume content was 46%. As ceramic precursor, a polysilazane (Durazane 1800, Merck, Darmstadt, Germany) was infiltrated via resin transfer moulding. As curing agent, 1 wt.% of dicumyl peroxide (Alfa Aesar, Kandel, Germany) was added to the polysilazane. After curing at 260 °C, the pyrolysis took place in a nitrogen atmosphere at temperatures above 1100 °C. Polymer infiltration and pyrolysis were carried out eight times until a residual porosity of less than 5% was achieved. The surfaces of the plate were grinded in the end. The manufacturing process is described in more detail elsewhere [34,35].

Three CMC plates were coated with 300 µm of silicon bond coat. The coating was applied in an Oerlicon Metco Multicoat facility with a TriplexPro210 mounted on a six-axis robot (Oerlicon Metco, Wholen, Switzerland). Metco 6157 (Yb₂Si₂O₇) and Metco 4810 (Si), also provided by Oerlicon Metco, were used for the coating manufacture. After the bond coat application, the surfaces of two of the three plates (specimen type 2 and 3, ST2 and ST3) were structured by a TruMark 5020 Nd:YAG laser (Trumpf, Ditzingen, Germany) with a maximum peak power of 15 KW and a wavelength of 1062 nm. The remaining sample (specimen type 1, ST1) serves as a reference to determine the interface fracture toughness of the original bond coat surface. The pattern geometry on ST2 and ST3, as well as the laser process parameter, are presented in Figure 1 and Table 1. The introduced grid structure consists of bridges, which are inversely created by basin-like laser ablation from areas with dimensions of 400 µm × 400 µm. The two investigated structures ST2 and ST3 differ in the width of the bridges, which is 50 µm for ST2 and 200 µm for ST3. The two structures were investigated to show the influence of the bridge's width on the interface toughness. To prevent oxide formation, the samples got structured under the inert gas argon.

Table 1. Laser parameters for structures on ST2 and ST3.

Pulse Length (ns)	Power (kW)	Frequency (kHz)	Laser Velocity (mm/s)	Spot Diameter (µm)	Line Offset (µm)
100	12	20	100	40	20

2.2. Characterization

The roughness of all three bond coats was analysed by a laser confocal microscope (VK-9700, Keyence, Neu-Isenburg, Germany). To determine the roughness, the plates ST1-ST3 were analysed by line scans with a z-axis resolution of 1 nm and a step width of 7 nm. To test the interface toughness of the bond coat/topcoat interface, the methodology proposed by Kakisawa et al. [33] was used. Specimens of dimension 4 mm × 3 mm, suited to the miniaturized test setup, were cut from the original plates of dimension 100 mm × 40 mm.

For the original test, several preparation steps, like Knoop indentation for pre-crack introduction, were necessary before a notch of 500 µm length was cut along the interface of interest. For the interface toughness test in this present work, the preparation got adapted by skipping the Knoop indentation and pre-crack introduction, while an enlarged notch of 1.7 mm length was cut by a diamond blade saw with a blade thickness of 100 µm. To prevent an early failure of the remaining topcoat, a 250 µm thick alumina plate was attached to the topcoat surface. A sketch of the test setup and a cross section of a specimen with an attached stiffener is presented in Figure 2.

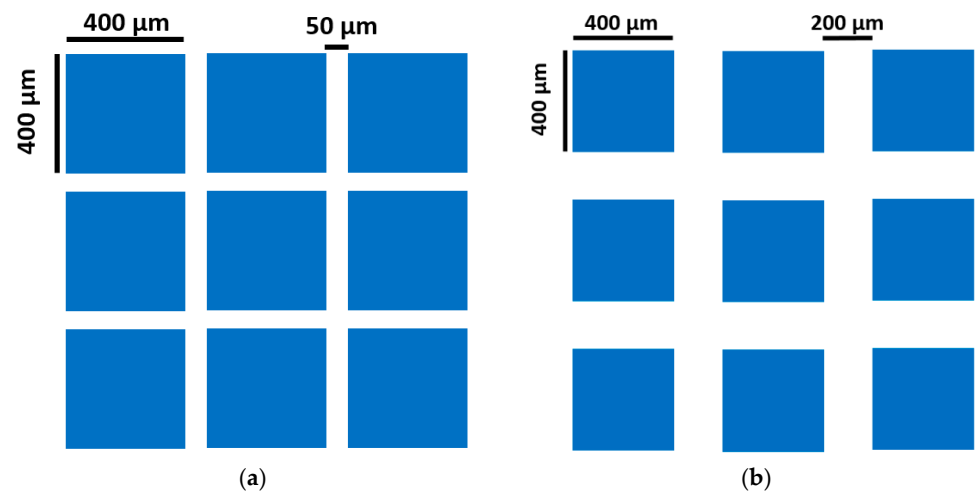


Figure 1. Outline of the laser structuring performed on (a) ST2 and (b) ST3. Basins created by laser ablation are indicated by color.

The adapted interface toughness test setup is illustrated in Figure 3. To immobilise the specimen, the sample was clamped vertically on the substrate side. The displacement of the coating during the test was observed by a laser distance measurement, while the pressure load is recorded by a load cell with a capacity of 50 N. The interface itself is observed and filmed by a light microscope to determine the exact time of the crack formation. To test the interface toughness of the samples, the 0.5 mm thick wedge-shaped tool with a wedge angle of 2θ of 17.6° gets inserted into the notch with a speed of $12 \mu\text{m/s}$. This wedge insertion results in a cantilever-like bending of the coating in the notch part, providing a stress concentration in near mode I at the crack tip. When the stress intensity on the tip is bigger than the interface toughness, a crack will propagate along the interface and delaminate the topcoat from the bond coat. Because all measurements (video observation, displacement, and pressure load) were started at the same time, it was possible to determine the pressure load and displacement from the measured curves at the moment of crack formation. Together with the notch length and the wedge angle, these two sets of values are necessary to calculate the initial interface toughness.

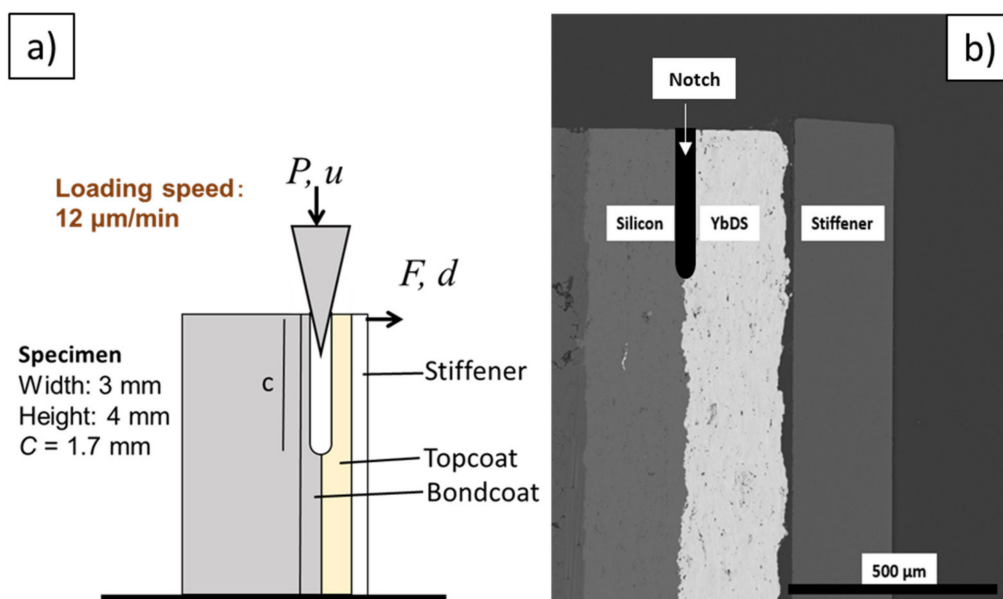


Figure 2. Draft of the original test setup (a) and a SEM picture of a prepared sample for the interface toughness test (b).

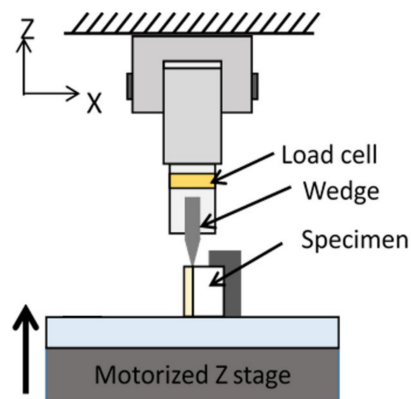


Figure 3. Adapted test setup for the interface toughness test.

3. Results and Discussion

After the laser structuring of the specimen ST2 and ST3, the roughness was measured for all three specimen types. 3D illustrations of an unstructured bond coat (ST1) and ST2, exemplary for the grid structures, are presented in Figure 4, while the determined roughness is presented in Table 2. From Figure 4, it can be seen that the height of the bridges is similar to the height of the asperities of the original bond coat.

Table 2. Determined roughness values of Specimen type 1–3.

Structure	Structure	R_v (μm)	R_z (μm)	R_c (μm)	R_a (μm)
ST1	ST1	28	78	43	7
ST2 (50 μm)	ST2 (50 μm)	34	82	60	11
ST3 (200 μm)	ST3 (200 μm)	56	95	69	10

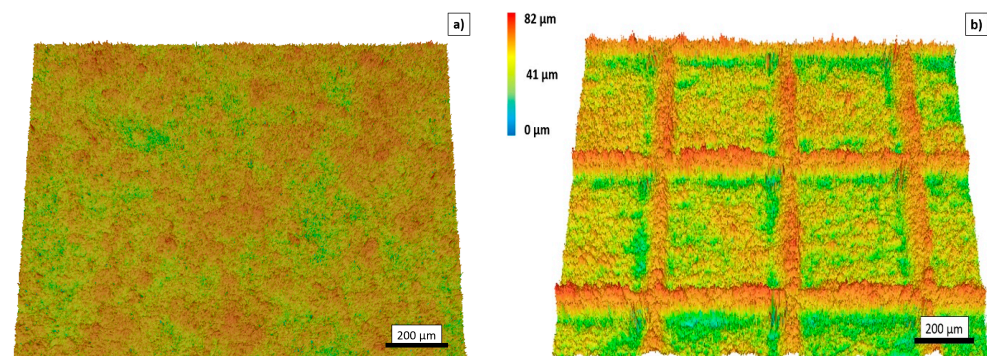


Figure 4. 3D illustrations of an unstructured bond coat (a) and an exemplary grid structure (b).

The results of the roughness measurement show that the roughness of the structured specimen (ST2 and ST3) is larger compared to the unstructured sample (ST1). The arithmetic mean roughness R_a increases from 7 to 10 and 11 μm , and the average height R_c increases from 43 to 60 and 69 μm . An increase in the maximum profile height R_z and profile depth R_v can also be observed.

By comparing the R values in Table 2, it is noticeable that the silicon bond coat already shows a rather high roughness before texturing, and the R_z value increases only slightly afterwards. When looking at the line profiles of the unstructured or structured bond coat in Figure 5, it can be observed that there are already some peaks and valleys in the unstructured bond coat, which might explain the high R_z value in the unstructured samples. However, in comparison with the structured surface (Figure 5b), these peaks only occur isolated, while the structures regularly reach a height of about 100 μm . Therefore, it can be assumed that, due to the different nature of the surface textures, the R_z values are not best

suitable to describe average properties of, e.g., the majority area of the sample surface. In summary, the introduced laser structures cause an increase in the roughness.

Microstructure images of the interfaces of all three samples (ST1 to ST3) before the tests are presented in Figure 6. The images show that all three bond coats are covered with the topcoat material YbDS without larger pores and cracks at the interface. These observations suggest that no weak point is present at the interface after the coating process. By comparing the height of the bridge structures taken from the cross sections after the coating process (Figure 6) with the height of the bridges taken from the line profile of the original structure (Figure 5b), it becomes obvious that the height of the bridges reduced from 100 μm to roughly 30 μm only. This can most probably be attributed to an erosive process from impinging particles in the thermal spray deposition of the ceramic top coat. This strong erosion should be considered in further tests. Furthermore, a micro roughness can be observed in the basin-like structures, which seems larger in comparison to the roughness of the unstructured interfaces. Therefore, it can be expected that this micro roughness, together with the bridge structures, may contribute to an improved adhesion of the layers.

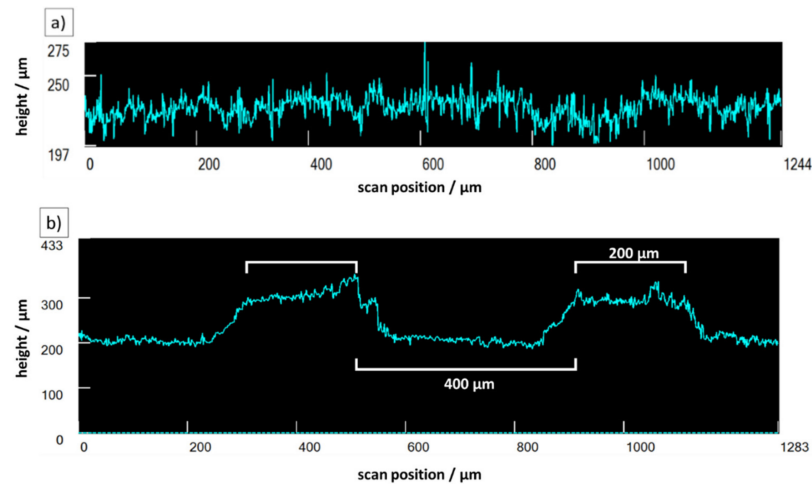


Figure 5. Line profiles of an unstructured ST1 (a) and a lattice-structured ST3 (b) silicon bond coat with 200 μm wide bridges and 400 μm basin structures, recorded by confocal microscopy.

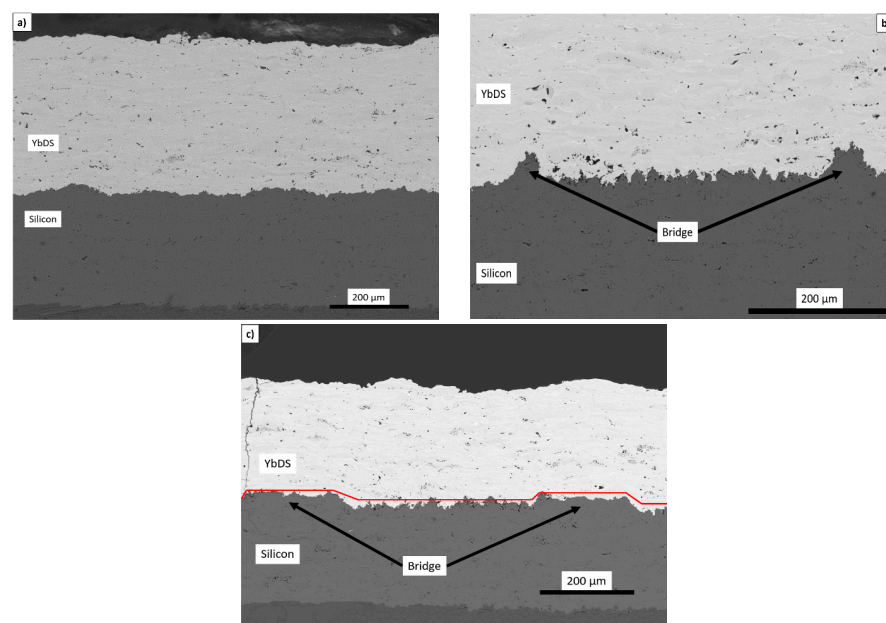


Figure 6. Bond coat/topcoat interface of specimen type 1 (a), specimen type 2 (b) and specimen type 3 (c) before the interface toughness test.

In a first step of the interface toughness calculation, the critical bending load F was calculated from the force equilibrium between the wedge and the specimen at the moment before cracking (Figure 7).

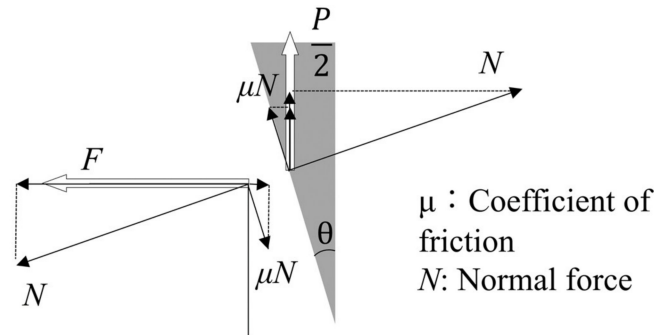


Figure 7. Force equilibrium between specimen und wedge.

As presented in Equations (1) and (2), the wedge load P and the critical bending load F can be divided into a force responsible for the crack opening, and a vertical working friction part, where N is the normal force acting on the wedge. Because the surface of the notch is very smooth and much harder than the metallic wedge, the friction is very small and is neglected in the present case. With the assumption of the negligible friction, the wedge load P and the critical bending load F can be combined in Equation (3), with A as a conversion factor between P and F . With this information, the interface toughness Γ can be calculated by integrating Equation (3) into Equation (4), where θ is the wedge angle (8.8°), b the specimen width (3 mm), and L the length of the notch.

$$\frac{P}{2} = N(\sin \theta + \mu \cos \theta) \quad (1)$$

$$F = N(\cos \theta - \mu \cos \theta) \quad (2)$$

$$F = \frac{1 \cos \theta}{2 \sin \theta} P = A \times P \quad (3)$$

$$\Gamma = \frac{3F\delta}{2bL} = \frac{3AP\delta}{2bL} \quad (4)$$

Besides the loads P and F , the notch displacement δ was calculated by the relation of the bending load F and the displacement as described in Equation (5).

$$F = \frac{3\overline{E'I}}{L^3} \delta \quad (5)$$

To calculate the displacement, the equivalent bending stiffness $\overline{E'I}$ must be determined. With the notations for the thicknesses of the bended layers, h_A and h_B , given in Figure 8 and the corresponding Young's moduli in plane strain condition, E'_A and E'_B , Equation (6) gives the position of the neutral axis η_0 . The equivalent bending stiffness then can be described as given in Equation (7). As proof that the stiffener does not detach from the sample as a result of the experiment, macroscopic and microscopic images of a tested sample are presented in Figure 9.

$$\eta_0 = \frac{E'_A h_A^2 + E'_B h_B^2 + 2E'_A h_A h_B}{2(E'_A h_A + E'_B h_B)} \quad (6)$$

$$\overline{E'I} = \frac{b}{3} \left[E'_A \left\{ (-\eta_0 + h_B + h_A)^3 - (-\eta_0 + h_B)^3 \right\} + E'_B \left\{ (-\eta_0 + h_B)^3 - (-\eta_0)^3 \right\} \right] \quad (7)$$

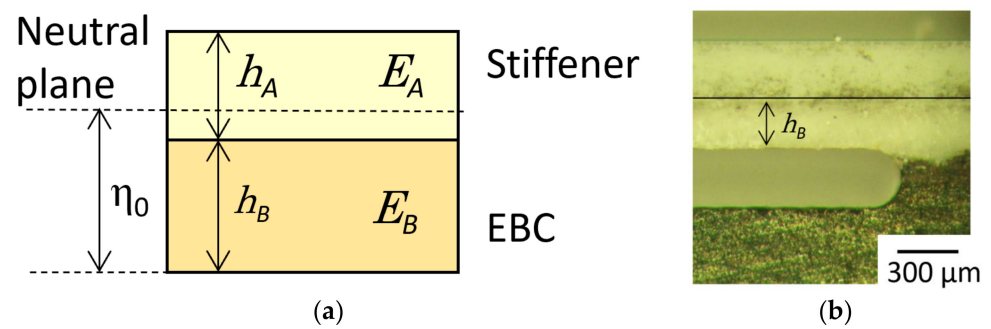


Figure 8. Additional information for the determination of the equivalent bending stiffness in a sketch (a) and a cross section (b).

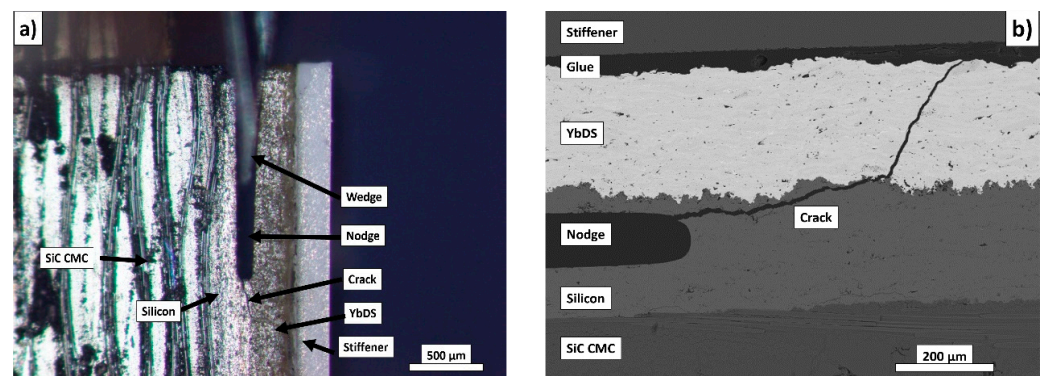


Figure 9. Macroscopic (a) and microscopic (b) pictures of a testes sample with attached stiffener.

The Young's moduli $E'A$ with 380 GPa and $E'B$ with 126.37 GPa for the alumina stiffener (A) and the YbDS topcoat (B) were determined in an indentation test with a load of 490 mN from the load displacement curve. E' was calculated by the Oliver Pharr method with Equation (8), a Poisson's ratio ν of 0.3 and E with 115 GPa.

$$E' = \frac{E}{1 - \nu^2} \quad (8)$$

The interface toughness can now be calculated by integrating Equation (5) into Equation (4) to Equation (9):

$$\Gamma = \frac{3AP_1\delta_1}{2bL} = \frac{L^2 A^2 P_1^2}{2bE'I} \quad (9)$$

The measured values and the results are summarized together with their error widths in Table 3. It can be determined that the interfacial toughness is increased by about 70% from 8.6 to 13.8 and 14.7 J/m², respectively. The interfacial toughness of the sample with unstructured interface is (8.6 ± 4.7 J/m²), which is in the range of other published papers (4–6.4 J/m²) if the standard deviation from the multiple evaluation is included [32,36]. The height of this error width can be attributed to the larger measurement deviations of the critical loads P and the groove lengths L .

Table 3. Measured displacement, load, notch length and calculated interface toughness for all sample types.

Sample	h_A	h_B	η_0	$E'I$	Load (P)	Length (L)	Interface Toughness (Γ)
	μm	μm	μm	Nm^2	N	μm	J/m^2
ST1 (Baseline)	287 ± 23	292 ± 21	367 ± 14	0.01	3.59 ± 1.37	1900 ± 190	8.62 ± 4.7
ST2 (50 μm)	272 ± 21	270 ± 16	344 ± 18	0.01	4.89 ± 0.82	1585 ± 88	14.7 ± 3.41
ST3 (200 μm)	271 ± 17	262 ± 16	337 ± 18	0.01	4.55 ± 1.09	1669 ± 34	13.8 ± 5.38

The interfaces and crack paths in a structured (ST3) and unstructured (ST1) specimen after the test are presented in Figure 10. By observing the crack paths, it is noticeable that at the beginning, the cracks generally follow the orientation of the interface, and the actual delamination shows an offset from the interface by 10–20 μm within the bond coat. In the unstructured sample (Figure 10a, arrows), it can be observed that the crack after following the interface bends into the topcoat for a short distance and then returns to the previous level in the silicon bond coat. In the structured samples (Figure 10b), it can be noticed that the crack initially runs parallel to the interface and preferentially deflects into the topcoat layer when striking a bridge structure. From the observation of cracks initially running within the bond coat layer, it can be concluded that the toughness calculated from the measurement results do not strictly reflect the pure interfacial toughness, as only the energy for the crack initiation is considered. Instead, it can be concluded that the determined values rather represent the initial fracture toughness of the bond where the crack starts to propagate from the notch tip into the coating material.

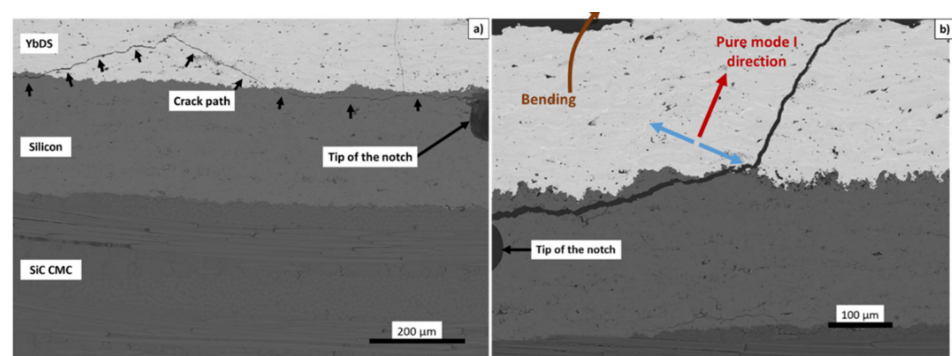


Figure 10. Interface and course of cracking of an unstructured (a) and a structured (b) specimen after the interface toughness test.

The difference in the calculated values between unstructured and structured samples therefore needs to be attributed to a change in the bond coat properties in the vicinity of the interface, which could be correlated to the effect of laser texture. Previous work has shown that the use of a laser can cause sintering of the material or improve splat adhesion [37–39]. This consolidation may result in the higher toughness of the material. Since the crack runs near the interface, the crack propagation is also more hindered in the laser affected areas than in the unstructured bond coat.

The observation of cracks, kinking into the top coat and returning into the bond coat, shown exemplarily in Figure 10, indicates a higher fracture toughness of the YbDS compared to the silicon bond coat. Additionally, it is concluded that the toughness of the interface is higher than the fracture toughness of the two materials. This is due to the observation that the crack runs only over very short distances at the interface. In addition, it can be assumed that the crack propagation along the interface is further impeded by a better mechanical interlocking at the structured interface, which would also further increase the already high toughness. Therefore, the following ranking of the fracture toughness can be established: The interface toughness is higher than the fracture toughness of the YbDS topcoat, while the fracture toughness of the structured silicon bond coat is lower. The fracture toughness of the untreated bond coat seems to be the lowest.

By more detailed observation of the crack propagation, starting from the tip of the notch, it is presumed that the cracks propagate along the splat boundaries in the bond coat toward the interface, and enter the topcoat with a steep angle where the energy release rate becomes the largest. As described by He et al. [40], the crack follows the mode I stress direction into the topcoat (Figure 10b) caused by the bending of the inserted wedge.

Thirty samples (10 per sample type) have been fully delaminated to analyse the overall crack paths. It was observed that the crack in the unstructured samples kinks significantly earlier into the topcoat to a total failure than in the structured samples. No difference was

noticeable between the specimen of the two structure types. Based on this observation, it may be assumed that the laser-structuring is partly suppressing a kinking of the crack into the topcoat to early failure. As this tendency is similar for both types of structured specimen, which only differ in the width of the bridges between the basin-like structures, it may also be assumed that this is more correlated to the interface structure of the basin-like regions.

For a better understanding of the crack paths, both crack surfaces of a completely delaminated structured sample (ST3) were analysed in more detail. The open crack surfaces (top and bottom) are shown in Figure 11. The appearance of different contrasts, which were identified by the energy-dispersive X-ray spectroscopy (EDS) as silicon (dark grey) and YbDS (light grey), indicates that the crack runs through both layer materials in a cohesive failure. In addition, it can be concluded that the crack at least partially follows the structured interface, since cracking at the interface region of the basin-like structures is identified from contrast change (Figure 11a) and a wave structure (Figure 11b) observed in the red marked areas.

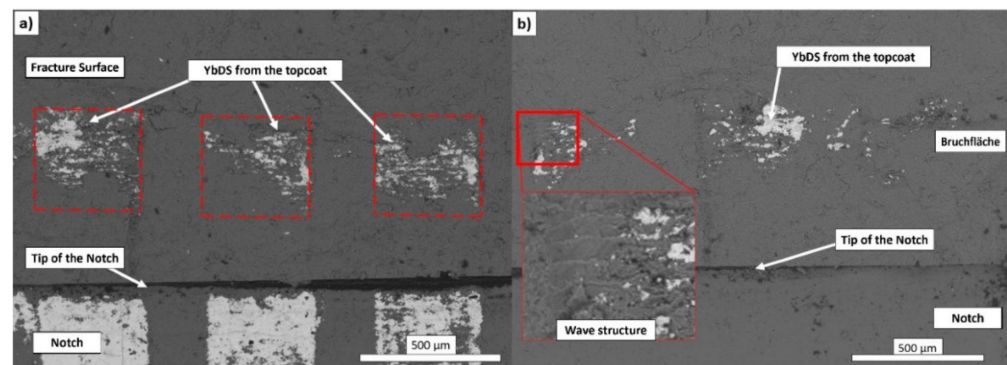


Figure 11. Fractured surfaces of the layer side (a) and the substrate side (b) of a completely delaminated, ST3-structured sample with red marked positions of the basin- and wave-like structures.

A repeated switching of crack path between two interfaces in multi-layered coating systems was reported from Kim et al. [41] and Kawai et al. [36] in shear mode loading where fracture toughness of the interfaces involved were similar or kinking was fostered by pegs. A repeated switching of crack path between interface and adjacent coating layer in coating systems with patterned interface was reported from Kromer et al. [17] and Kim et al. [42] where kinking is fostered at regular asperities of the patterned interface. Commonly, an increase of the effective adhesion strength is reported, which is attributed to delamination not purely arising at the weakest interface. The macroscopic fracture toughness could be described by an average of toughness of the contributing crack areas. Even though a clear identification of the microscopic features fostering the repeated switching of the crack path in the basin-like structures can hardly be drawn from the experiments in the current study, it is likely that the effective adhesion strength of the coatings is improved in case of the structured bond coat due to both the enhanced fracture toughness of the interface near bond coat region and the crack partly propagating within the YbDS top coat.

4. Conclusions

Two different laser structures were processed into a silicon bond coat surface and covered by an YbDS topcoat. The introduced grid structures consist of bridges created by ablation of basin-like $400\ \mu\text{m} \times 400\ \mu\text{m}$ structures. The investigated structures differ in the width of the created bridges, which was $50\ \mu\text{m}$ for the first and $200\ \mu\text{m}$ for the second structure. A new testing method was used to compare the interface toughness of an untreated and the textured specimens. The analysis of the crack path after testing indicated that the values calculated from the measurement results do not strictly reflect the pure interface toughness. Instead, it can be assumed that the observed values can be rather interpreted as the initial fracture toughness of the bond coat volume around the

interface. Nevertheless, the results of the toughness test exhibit that the method developed by Kakisawa et al. allows precise positioning of the crack initiation compared to other methods and shows a strong increase of the crack resistance in the bond coat by the laser structuring (14.6 J/m^2) compared to an unstructured specimen (8 J/m^2).

Different contributions could possibly explain the observed behaviours. It is assumed that the laser treatment leads to a densification and sintering of the silicon bond coat, which impedes the crack propagation in this area. This impediment, as well as a kinking into the topcoat, could also be intensified by the introduced structures, which could initiate out of plane stresses. It is assumed that these stresses counteract the pure mode I stresses from the bending and direct the crack back into the bond coat material. In addition, it is estimated that the densified bond coat interface exhibits a fracture toughness similar to the YbDS topcoat. The occurrence of the mixed cohesive failure in both coating materials could also contribute to explain the improved toughness and crack path. At this point, the exact cause cannot be identified. Therefore, further test series increased measured toughness attributed to increased toughness of the adjacent BC layer with even more precise notch placements to introduce stress peaks in the contributing layers. In this way, various failure modes and specific crack propagation could be initiated, which could be compared with the results of this study. Beyond this, comprehensive studies utilizing, e.g., nano indentation methods and screening the impact of dimensional variations of the grid structures will help to discriminate more clearly the contributions from materials and geometrical origin.

Author Contributions: Conceptualization, M.W. and D.E.M.; methodology, M.W. and H.K.; validation, M.W., H.K., and D.E.M.; investigation, M.W.; resources, F.S.; writing—original draft preparation, M.W.; writing—review and editing, M.W., H.K., D.E.M., F.S., and R.V.; visualization, M.W. and H.K.; supervision, D.E.M. and R.V.; funding acquisition, R.V. All authors have read and agreed to the published version of the manuscript.

Funding: This work was financially supported by the Helmholtz Association of German Research Centers.

Data Availability Statement: The data presented in this study are available in the article.

Acknowledgments: We would like to thank T. Kawano for technical assistance.

Conflicts of Interest: The authors declare no conflict of interest.

References

1. Padture, N.P. Advanced structural ceramics in aerospace propulsion. *Nat. Mater.* **2016**, *15*, 804–809. [[CrossRef](#)] [[PubMed](#)]
2. Miller, R.A. Thermal barrier coatings for aircraft engines: History and directions. *JTST* **1997**, *6*, 35–42. [[CrossRef](#)]
3. Bansal, N.P.; Lamon, J. *Ceramic Matrix Composites. Materials, Modeling and Technology*; Wiley: Hoboken, NJ, USA, 2015; ISBN 978-1-118-23116-6.
4. Koff, B. Spanning the globe with jet propulsion. In Proceedings of the 21st Annual Meeting and Exhibit, Arlington, VA, USA, 30 April–2 May 1991.
5. Belmonte, M. Advanced ceramic materials for high temperature applications. *Adv. Eng. Mater.* **2006**, *8*, 693–703. [[CrossRef](#)]
6. Jiang, D.; Zhang, L. High temperature ceramic matrix composites 8. In Proceedings of the A collection of papers presented at the HTCMC-8 Conference, Xi'an, China, 22–26 September 2013.
7. Perepezko, J.H. Materials science. The hotter the engine, the better. *Science* **2009**, *326*, 1068–1069. [[CrossRef](#)] [[PubMed](#)]
8. Eaton, H.E.; Linsey, G.D. Accelerated oxidation of SiC CMC's by water vapor and protection via environmental barrier coating approach. *J. Eur. Ceram. Soc.* **2002**, *22*, 2741–2747. [[CrossRef](#)]
9. Lee, K.N. Environmental barrier coatings for SiC f/SiC. In *Ceramic Matrix Composites: Materials, Modeling and Technology*; Bansal, N.P., Lamon, J., Eds.; Wiley: Hoboken, NJ, USA, 2015; pp. 430–451, ISBN 9781118832998.
10. Yang, X.; Zhao-hui, C.; Feng, C. High-temperature protective coatings for C/SiC composites. *J. Asian Ceram. Soc.* **2014**, *2*, 305–309. [[CrossRef](#)]
11. Xu, Y.; Hu, X.; Xu, F.; Li, K. Rare earth silicate environmental barrier coatings: Present status and prospective. *Ceram. Int.* **2017**, *43*, 5847–5855. [[CrossRef](#)]
12. Lee, K.N.; Eldridge, J.I.; Robinson, R.C. Residual stresses and their effects on the durability of environmental barrier coatings for SiC ceramics. *J. Am. Ceram. Soc.* **2005**, *88*, 3483–3488. [[CrossRef](#)]
13. Mauer, G.; Jarligo, M.O.; Mack, D.E.; Vaßen, R. Plasma-sprayed thermal barrier coatings: New materials, processing issues, and solutions. *JTST* **2013**, *22*, 646–658. [[CrossRef](#)]

14. Wolf, M.; Mack, D.E.; Guillon, O.; Vaßen, R. Resistance of pure and mixed rare earth silicates against calcium–magnesium–aluminosilicate (CMAS): A comparative study. *J. Am. Ceram. Soc.* **2020**, *281*, 472. [[CrossRef](#)]
15. Vaßen, R.; Jarligo, M.O.; Steinke, T.; Mack, D.E.; Stöver, D. Overview on advanced thermal barrier coatings. *Surf. Coat. Technol.* **2010**, *205*, 938–942. [[CrossRef](#)]
16. Bakan, E.; Marcano, D.; Zhou, D.; Sohn, Y.J.; Mauer, G.; Vaßen, R. Yb₂Si₂O₇ Environmental barrier coatings deposited by various thermal spray techniques: A preliminary comparative study. *JTST* **2017**, *26*, 1011–1024. [[CrossRef](#)]
17. Kromer, R.; Costil, S.; Verdy, C.; Gojon, S.; Liao, H. Laser surface texturing to enhance adhesion bond strength of spray coatings—Cold spraying, wire-arc spraying, and atmospheric plasma spraying. *Surf. Coat. Technol.* **2018**, *352*, 642–653. [[CrossRef](#)]
18. Courapied, D.; Kromer, R.; Berthe, L.; Peyre, P.; Costil, S.; Cormier, J.; Boustie, M.; Milhet, X. Laser adhesion test for thermal sprayed coatings on textured surface by laser. *J. Laser Appl.* **2016**, *28*, 22509. [[CrossRef](#)]
19. Foldyna, J.; Sitek, L.; Ščučka, J.; Martinec, P.; Valíček, J.; Páleníková, K. Effects of pulsating water jet impact on aluminium surface. *J. Mater. Process. Technol.* **2009**, *209*, 6174–6180. [[CrossRef](#)]
20. Meijer, J.; Du, K.; Gillner, A.; Hoffmann, D.; Kovalenko, V.S.; Masuzawa, T.; Ostendorf, A.; Poprawe, R.; Schulz, W. Laser machining by short and ultrashort pulses, state of the art and new opportunities in the age of the photons. *Cirp Ann.* **2002**, *51*, 531–550. [[CrossRef](#)]
21. Garcia-Alonso, D.; Serres, N.; Demian, C.; Costil, S.; Langlade, C.; Coddet, C. Pre-/during-/post-laser processes to enhance the adhesion and mechanical properties of thermal-sprayed coatings with a reduced environmental impact. *JTST* **2011**, *20*, 719–735. [[CrossRef](#)]
22. Abt, M.; Wolf, M.; Feldhoff, A.; Overmeyer, L. Combined spray-coating and laser structuring of thermoelectric ceramics. *J. Mater. Process. Technol.* **2020**, *275*, 116319. [[CrossRef](#)]
23. Sommer, M.; Fornalczyk, G.; Mumme, F. Development of a laser structuring process for ceramic coatings on injection molding tools produced by MOCVD. *KEM* **2019**, *809*, 303–308. [[CrossRef](#)]
24. Pedrini, G.; Martínez-García, V.; Weidmann, P.; Wenzelburger, M.; Killinger, A.; Weber, U.; Schmauder, S.; Gadow, R.; Osten, W. Residual stress analysis of ceramic coating by laser ablation and digital holography. *Exp. Mech.* **2016**, *56*, 683–701. [[CrossRef](#)]
25. Gatzen, C.; Mack, D.E.; Guillon, O.; Vaßen, R. Surface roughening of Al₂O₃/Al₂O₃-ceramic matrix composites by nanosecond laser ablation prior to thermal spraying. *J. Laser Appl.* **2019**, *31*, 22018. [[CrossRef](#)]
26. Charalambides, P.G.; Cao, H.C.; Lund, J.; Evans, A.G. Development of a test method for measuring the mixed mode fracture resistance of bimaterial interfaces. *Mech. Mater.* **1990**, *8*, 269–283. [[CrossRef](#)]
27. Kawashita, L.F.; Moore, D.R.; Williams, J.G. The measurement of cohesive and interfacial toughness for bonded metal joints with epoxy adhesives. *Compos. Interfaces* **2005**, *12*, 837–852. [[CrossRef](#)]
28. Yoon, S.H.; Hong, C.S. Modified end notched flexure specimen for mixed mode interlaminar fracture in laminated composites. *Int. J. Fract.* **1990**, *43*, R3–R9. [[CrossRef](#)]
29. Davidson, B.D.; Sundaraman, V. A single leg bending test for interfacial fracture toughness determination. *Int. J. Fract.* **1996**, *78*, 193–210. [[CrossRef](#)]
30. Zhu, Q.; He, W.; Chen, L.; Zhu, J.; Hao, W. Interfacial toughness evaluation of thermal barrier coatings by bending test. *Theor. Appl. Mech. Lett.* **2018**, *8*, 3–6. [[CrossRef](#)]
31. Berthe, L.; Arrigoni, M.; Boustie, M.; Cuq-Lelandais, J.P.; Broussillou, C.; Fabre, G.; Jeandin, M.; Guipont, V.; Nivard, M. State-of-the-art laser adhesion test (LASAT). *Nondestruct. Test. Eval.* **2011**, *26*, 303–317. [[CrossRef](#)]
32. Kakisawa, H.; Nishimura, T. A method for testing the interface toughness of ceramic environmental barrier coatings (EBCs) on ceramic matrix composites (CMCs). *J. Eur. Ceram. Soc.* **2018**, *38*, 655–663. [[CrossRef](#)]
33. Kakisawa, H.; Nishimura, T. A modified simple interface fracture test for ceramic environmental barrier coating (EBC) on ceramics matrix composite (CMC). *J. Ceram. Soc. Jpn.* **2018**, *38*, 655–663. [[CrossRef](#)]
34. Hömig, S.; Süß, F.; Jain, N.; Jemmali, R.; Behrendt, T.; Mainzer, B.; Koch, D. Evaluation of preparation and combustion rig tests of an effusive cooled SiC/SiCN panel. *Int. J. Appl. Ceram. Technol.* **2020**, *139*, 325. [[CrossRef](#)]
35. Mainzer, B.; Frie, M.; Jemmali, R.; Koch, D. Development of polyvinylsilazane-derived ceramic matrix composites based on Tyranno SA3 fibers. *J. Ceram. Soc. Jpn.* **2016**, *124*, 1035–1041. [[CrossRef](#)]
36. Kawai, E.; Kakisawa, H.; Kubo, A.; Yamaguchi, N.; Yokoi, T.; Akatsu, T.; Kitaoka, S.; Umeno, Y. Crack initiation criteria in EBC under thermal stress. *Coatings* **2019**, *9*, 697. [[CrossRef](#)]
37. Qian, B.; Shen, Z. Laser sintering of ceramics. *J. Asian Ceram. Soc.* **2013**, *1*, 315–321. [[CrossRef](#)]
38. Ganz, D.; Gasparro, G.; Aegerter, M.A. Laser sintering of SnO₂: Sb sol-gel coatings. *J. Sol-Gel Sci. Technol.* **1998**, *13*, 961–967. [[CrossRef](#)]
39. Chen, A.-N.; Wu, J.-M.; Liu, K.; Chen, J.-Y.; Xiao, H.; Chen, P.; Li, C.-H.; Shi, Y.-S. High-performance ceramic parts with complex shape prepared by selective laser sintering: A review. *Adv. Appl. Ceram.* **2018**, *117*, 100–117. [[CrossRef](#)]
40. He, M.-Y.; Bartlett, A.; Evans, A.G.; Hutchinson, J.W. Kinking of a crack out of an interface: Role of in-plane stress. *J. Am. Ceram. Soc.* **1991**, *74*, 767–771. [[CrossRef](#)]
41. Kim, S.-S.; Liu, Y.-F.; Kagawa, Y. Evaluation of interfacial mechanical properties under shear loading in EB-PVD TBCs by the pushout method. *Acta Mater.* **2007**, *55*, 3771–3781. [[CrossRef](#)]
42. Kim, W.S.; Lee, J.J. Interfacial fracture toughness measurement and improvement for composite/metal interfaces. *ICCM Int. Conf. Compos. Mater.* **2009**, *222*, 1–10.